

Quantitative multi-phase-field modeling of non-isothermal solidification in hexagonal multicomponent alloys

*Yong-biao Wang¹, Ming-guang Wei¹, **Xin-tian Liu¹, Cong Chen¹, Jian-xiu Liu¹, Yu-juan Wu², Shuai Dong^{2,3}, and Li-ming Peng²

1. Henan Key Laboratory of Intelligent Manufacturing of Mechanical Equipment, Zhengzhou University of Light Industry, Zhengzhou 450002, China

2. National Engineering Research Center of Light Alloy Net Forming and State Key Laboratory of Metal Matrix Composite, Shanghai Jiao Tong University, Shanghai 200240, China

3. Luoyang Institute of Special Materials Research, Luoyang 471600, Henan, China

Abstract: A quantitative multi-phase-field model for non-isothermal and polycrystalline solidification was developed and applied to dilute multicomponent alloys with hexagonal close-packed structures. The effects of Lewis coefficient and undercooling on dendrite growth were investigated systematically. Results show that large Lewis coefficients facilitate the release of the latent heat, which can accelerate the dendrite growth while suppress the dendrite tip radius. The greater the initial undercooling, the stronger the driving force for dendrite growth, the faster the growth rate of dendrites, the higher the solid fraction, and the more serious the solute microsegregation. The simulated dendrite growth dynamics are consistent with predictions from the phenomenological theory but significantly deviate from the classical JMAK theory which neglects the soft collision effect and mutual blocking among dendrites. Finally, taking the Mg-6Gd-2Zn (wt.%) alloy as an example, the simulated dendrite morphology shows good agreement with experimental results.

Keywords: multi-phase-field model; non-isothermal solidification; polycrystalline; multicomponent alloys; dendrite growth; microstructure

CLC numbers: TP391.9

Document code: A

Article ID: 1672-6421(2022)03-263-12

1 Introduction

The phase-field method is versatile in describing and predicting the size, morphology, and spatial distribution of local structure during the evolution of a complex microstructure. Based on the Ginzburg-Landau theory of phase transitions, phase-field equations have been developed to consider the combined action of the phase-field variables, kinetics, applied external fields, and different thermodynamic driving forces. The numerical solution to the phase-field equations can reproduce the morphology and motion of interfaces in real-time, thus avoiding the explicit tracking of interface

positions^[1-3]. The method has been extensively used in the simulation of microstructure evolution during solidification.

In recent years, great progress has been made in understanding the mechanisms of solidification microstructure evolution using the phase-field method^[3-6]. Among these studies, WBM model^[7], KKS model^[8], and the multi-phase-field model^[9, 10] are most commonly used. Although these models can provide a good description of the solidification microstructure evolution in alloys, the problems of spurious kinetics and solute trapping are not resolved, which become non-trivial when the scale of interfacial thickness is considerably larger than the capillary length, thus limiting the simulation scale^[11]. To solve this problem, Karma et al.^[12, 13] proposed a quantitative model to cancel spurious kinetics effects, such as the interface stretching and surface diffusion arising from the interface width, which also guaranteed the local chemical equilibrium at the interface. An anti-trapping current was introduced into the model to adjust the

*Yong-biao Wang

Male, born in 1984, Ph.D., Lecturer. His research interest mainly focuses on the simulation of microstructure of lightweight alloys.

E-mail: wsbiaoyongwang@163.com

**Xin-tian Liu

E-mail: 2016026@zzuli.edu.cn

Received: 2021-07-24; Accepted: 2021-12-24

unbalanced solute distribution and avoid the abnormal solute trapping effect, which made it possible to quantitatively simulate the solidification alloys. To date, the Karma model has been extensively applied to the investigation of multi-dendritic growth^[14-17]. Ofori-Opoku et al.^[18] quantitatively reproduced the solute segregation and dendrite morphology at different growth stages. Nevertheless, they ignored the role of latent heat during dendritic growth. Subsequently, Chen et al.^[19] also predicted the effect of solute diffusion on dendrite growth during polycrystalline growth, and quantitatively analyzed the variation of tip velocity and concentration of different dendrite arms in the same dendrite. The model treated the temperature field using the "frozen temperature approximation". In the same way, Yang et al.^[20] and Gong et al.^[21] studied the effects of cooling rate and undercooling on the growth behavior of dendrites respectively, and found that the increase of both factors would lead to the increase of solid volume fraction and dendrite growth rate. Wu et al.^[22] studied the non-isothermal solidification of multi-dendritic growth. Ren et al.^[23] investigated dendrites impingement and coarsening, showing the free dendrite growth at initial solidification stages while the dendrite impingement at later stages, which would accompany significant latent heat release, slowing down the growth and promoting the coarsening of dendrites. However, the contribution of latent heat release to the growth kinetics of dendrites, such as dendrite growth rate, tip radius and solute distribution, has not been explicitly investigated. Most of the models mentioned above have either considered the isothermal case or used the frozen temperature approximation, while neglected the latent heat release and multi-dendrites interactions during solidification. Furthermore, most of these works were devoted to cubic alloys, while the simulation of hexagonal alloys started only very recently due to the complex anisotropy and diverse growth orientation^[24-26]. Therefore, the non-isothermal solidification model of hexagonal materials requires more research efforts.

In this study, to further understand the competitive growth of multi-dendrites during non-isothermal solidification, a phase-field model containing latent heat of solidification was established based on the Karma model, which introduced interaction energy to reflect the interaction between dendrites^[18]. The convergence study using different phase-field parameters was performed firstly. In this convergence study, the effects of spatial step and coupling coefficient on dendrite growth were quantitatively described, and the optimal stimulation parameters were obtained. The variation of solid fraction and growth rate under different Lewis coefficients and undercooling was revealed. The growth behavior of different dendrite arms during polycrystalline growth was analyzed. The simulation results were compared with the Johnson-Mehl-Avrami-Kolmogorov (JMAK) theory^[27-29], which further confirm the model's capability of describing the interaction between dendrites effectively. Finally, the solidification process of Mg-6Gd-2Zn (wt.%) alloy was simulated and compared with experimental results.

2 Phase-field model for non-isothermal and polycrystalline alloys

2.1 Temperature in non-isothermal solidification

A multicomponent dilute alloy's solidification process of N 's components consistent with equal specific heat c_p at constant pressure in the liquid and solid is considered, and the diffusion coefficient of solid solute is zero. Also, in this study, the dependence of the thermal diffusivities on the temperature T was taken into consideration. In sharp-interface equations, the T at the interface obeys Gibbs-Thomson relation as follows^[30]:

$$T = T_M + \sum_i^{N-1} m_i c_{1,i} - \Gamma \kappa - V_n / \mu_k \quad (1)$$

where T_M is the pure solvent's melting temperature, m_i is the liquidus slope of element i , $c_{1,i}$ is the element i concentration at the liquid side of interface, Γ is the Gibbs-Thomson coefficient, κ is the local interface curvature, V_n is the interface's normal velocity, μ_k is the linear kinetic coefficient.

To connect the sharp-interface and the following phase-field model, it's convenient to introduce the dimensionless temperature θ with respect to the temperature at equilibrium state:

$$\theta = \frac{T - T_0}{L / c_p} \quad (2)$$

where $T_0 = T_M + \sum m_i c_{1,i}^e$, $c_{1,i}^e$ is the value of equilibrium liquid concentration of element i , and L is the fusion's latent heat.

2.2 Phase-field model

In this work, a set of order parameter $\varphi_i(r,t)$ was introduced to describe different phases at the given location and time, which satisfied $-1 \leq \varphi_i \leq 1$, where $\varphi_i = -1$ represents the liquid, $\varphi_i = 1$ represents solid. Normally, the value φ_i is 1 while the other φ_j for $j \neq i$ is -1 with a specified orientation^[18] in the i -th grain of the solid-phase. The values of $\varphi_i(r,t)$ smoothly across the interface and grain boundaries are different. The supersaturation field $u_i(r,t)$ can characterize the solute concentration field $c_i(r,t)$:

$$u_i = \frac{1}{1 - k_i} \left[\left(\frac{2c_i / c_{1,i}^e}{1 + k_i - (1 - k_i)h(\varphi_i)} \right) - 1 \right] \quad (3)$$

where k_i is the solute partition coefficient of element i . $h(\varphi_i) = -1 + \sum (\varphi_i + 1)$ is an interpolation function varies between -1 and 1 .

The interfacial anisotropy is introduced, which can be expressed as:

$$a_s(\vec{n}) = 1 + \varepsilon_0 + \varepsilon_6 \cos[6(\phi - \phi_0)] \quad (4)$$

where $\varepsilon_0 = 0.008$, $\varepsilon_6 = 0.07$, ϕ is the angle of the interface normal of each grain with the x -axis, ϕ_0 is the angle between the crystallographic axis and x -axis.

The governing equations for the phase-field modeling of non-isothermal and polycrystalline solidification in dilute

alloys can finally be expressed as:

$$\begin{aligned} & \tau_0 \xi(\{u_i\}) a_s^2(\vec{n}) \partial_i \varphi_i \\ & = W_0^2 \nabla \cdot [a_s^2(\vec{n}) \nabla \varphi_i] + W_0^2 \sum_{m=x,y} \left[\partial_m \left(|\nabla \varphi_i|^2 a_s(\vec{n}) \frac{\partial a_s(\vec{n})}{\partial (\partial_m \varphi_i)} \right) \right] \\ & + \varphi_i - \varphi_i^3 - \lambda (1 - \varphi_i^2)^2 \left(\theta + \sum_{i=1}^{N-1} M_i u_i \right) - \frac{\partial f_{\text{int}}(\varphi_i)}{\partial \varphi_i} \end{aligned} \quad (5)$$

$$\begin{aligned} & \frac{[1 + k_i - (1 - k_i)h(\varphi_i)]}{2} \partial_i u_i \\ & = \nabla \cdot \left\{ \frac{[k_i D_{s,i} + D_{l,i} + (k_i D_{s,i} - D_{l,i})h(\varphi_i)]}{2} \nabla u_i - \vec{J}_{\text{AT}} \right\} \\ & + \frac{1}{2} [1 + (1 - k_i)u_i] \sum_i \partial_i \varphi_i \end{aligned} \quad (6)$$

$$\partial_t \theta = D_T \nabla^2 \theta + \frac{\partial_t \varphi_i}{2} \quad (7)$$

In Eq. (5), τ_0 and W_0 are the time and length scales used to non-dimensionalize, which represent a relaxation time and a measure of the interface width, respectively. λ is a dimensionless coupling parameter.

$$\xi(\{u_i\}) = \frac{1}{\text{Le}} + D_{\min} \sum_{i=1}^{N-1} \frac{[1 + (1 - k_i)u_i] M_i}{D_{1,i}} \quad (8)$$

where Le is the Lewis coefficient, D_{\min} represents the lowest diffusivity in the liquid, $M_i = d_0/d_i$, $d_0 = \Gamma/(L/c_p)$ is the thermal capillary length, $d_i = -\Gamma/[m_i(1 - k_i)c_{1,i}^e]$ is the chemical capillary length connected with element i , and $D_{v,i}$ is the element i solutal diffusivity in v phase with $v=1$ (s) for liquid (solid). It is noticed that as $i=N$, $D_{v,N} = D_T$ is the thermal diffusivity.

$f_{\text{int}}(\varphi_i)$ in Eq. (5) reflects the interaction energy between grains with different orientations, which prevents the overlap of grains. It follows the form of:

$$f_{\text{int}}(\varphi_i) = \sum_i \sum_{j \neq i} \alpha \left(\frac{1 + \varphi_i}{2} \right)^2 \left(\frac{1 + \varphi_j}{2} \right)^2 \quad (9)$$

where $\alpha=4$. For the two order parameters φ_1 and φ_2 , the interaction energy's shape is given in Fig. 1. As can be seen, the interaction energy within the grain ($\varphi_i=1$) and in the liquid phase ($\varphi_i=-1$) is 0. The interaction between dendrites occurs only at the interface.

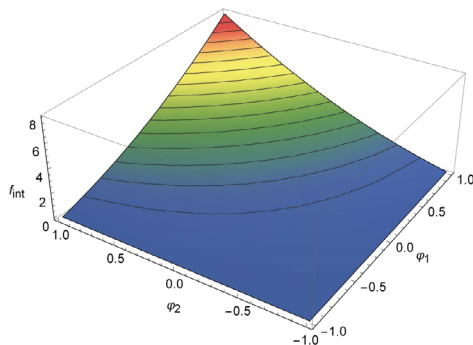


Fig. 1: Graph of interaction potential function between order parameter φ_1 and φ_2 . When φ_1 and φ_2 gradually approach 1, the interaction potential between the two dendrites will reach the maximum

For alloys solidification, the introduction of an anti-trapping current (\vec{J}_{AT}) in Eq. (6) can recover the S/L interface's local equilibrium. Furthermore, \vec{J}_{AT} can remove the abnormal phenomena when the capillary length is less than the interface width^[32]. According to solute diffusion in solid phase, \vec{J}_{AT} for polycrystalline alloys can be expressed by^[33]:

$$\vec{J}_{\text{AT}} = -\frac{1}{2\sqrt{2}} \left(1 - \frac{k_i D_{s,i}}{D_{l,i}} \right) [1 + (1 - k_i)u_i] \sum_i \partial_i \varphi_i \frac{\Delta \varphi_i}{|\Delta \varphi_i|} \quad (10)$$

2.3 Simulation parameters and numerical implementations

In this work, non-isothermal solidification of ternary alloys was mainly studied. The diffusion coefficient of solute in solid was ignored in the model, and all properties of material were supposed to be constant. When the width of the diffusion interface was smaller than the radius of curvature of the interface, but larger than the actual width of the solid-liquid interface, then the dynamic effect can be ignored, the model can be simplified to a sharp interface equation^[34, 35]. The governing equations of the phase field Eq. (5) and the solute conservation Eq. (6) were solved by the finite-difference method. The implicit method of alternating direction was adopted to discretize Eq. (7). The time step was set to $\Delta t = \Delta \tilde{x}^2 / (5\tilde{D}_T)$, where $\Delta \tilde{x} = \Delta x / W_0$ was the grid spacing, $W_0 = 10^{-7} \text{m}$, $\tilde{D}_T = D_T / D_{\min}$. In an 800×800 grid area, 30 randomly oriented crystals were used to simulate polycrystalline growth. A solid seed with radius of $R_1 = 4.0 W_0$ was set as the initiation of the simulation. Also, Neumann boundary condition was applied to all variables including φ_i , $\{u_i\}$ and θ . The initial dimensionless supersaturation $u_1 = u_2 = 0.65$, and the initial dimensionless temperature $\theta = -0.55$. For a ternary alloy, other calculation parameters were: $\Delta \tilde{x} = 0.8$, $\lambda = 10$, $k_1 = 0.35$, $k_2 = 0.16$, and $\text{Le} = 10$.

3 Simulated results and discussion

3.1 Simulation of polycrystalline growth into undercooled melt

Figure 2 shows the simulation results of random growth of 30 grains in undercooled melt. In the initial stage ($t=500 \Delta t$), these dendrites grow freely away from each other. Their solute and thermal diffusion fields do not overlap with other solute and thermal diffusion fields. Therefore, dendrites appear in symmetric shape in general, which is the same as that of single crystal growth. With solidification proceeding, the solute around the dendrite interacts with the thermal diffusion boundary layer and enters the collision stage. At $t=5,000 \Delta t$, it can be clearly observed from Figs. 2(a₂)-(d₂) that the dendrites compete and collide with each other during the growth process, resulting in deformation of dendrites. Moreover, a large amount of solutes and latent heat concentrate on space

between grains, which further aggravate the deformation of dendrites. Accompanied by dendritic growth, more and more solutes and latent heat are continuously released and accumulated. Hence, the growth of solid becomes very slow when the undercooled melt is completely consumed. In the interfacial region surrounded by dendrite arm, the solute is not easy to diffuse to the liquid phase, which results in the enrichment of solute in this area and the shrink of the necks of

dendrites in the root of primary dendrite arm. At $t=15,000 \Delta t$, the solidification almost stops, and the temperature distribution tends to become uniform due to thermal diffusion with very little heat generation. Meanwhile, due to the introduction of the interaction potential between the dendrites in the model, it can be found that even if the distance between the dendrites is very narrow to each other during the solidification process, there is no direct contact between grains.

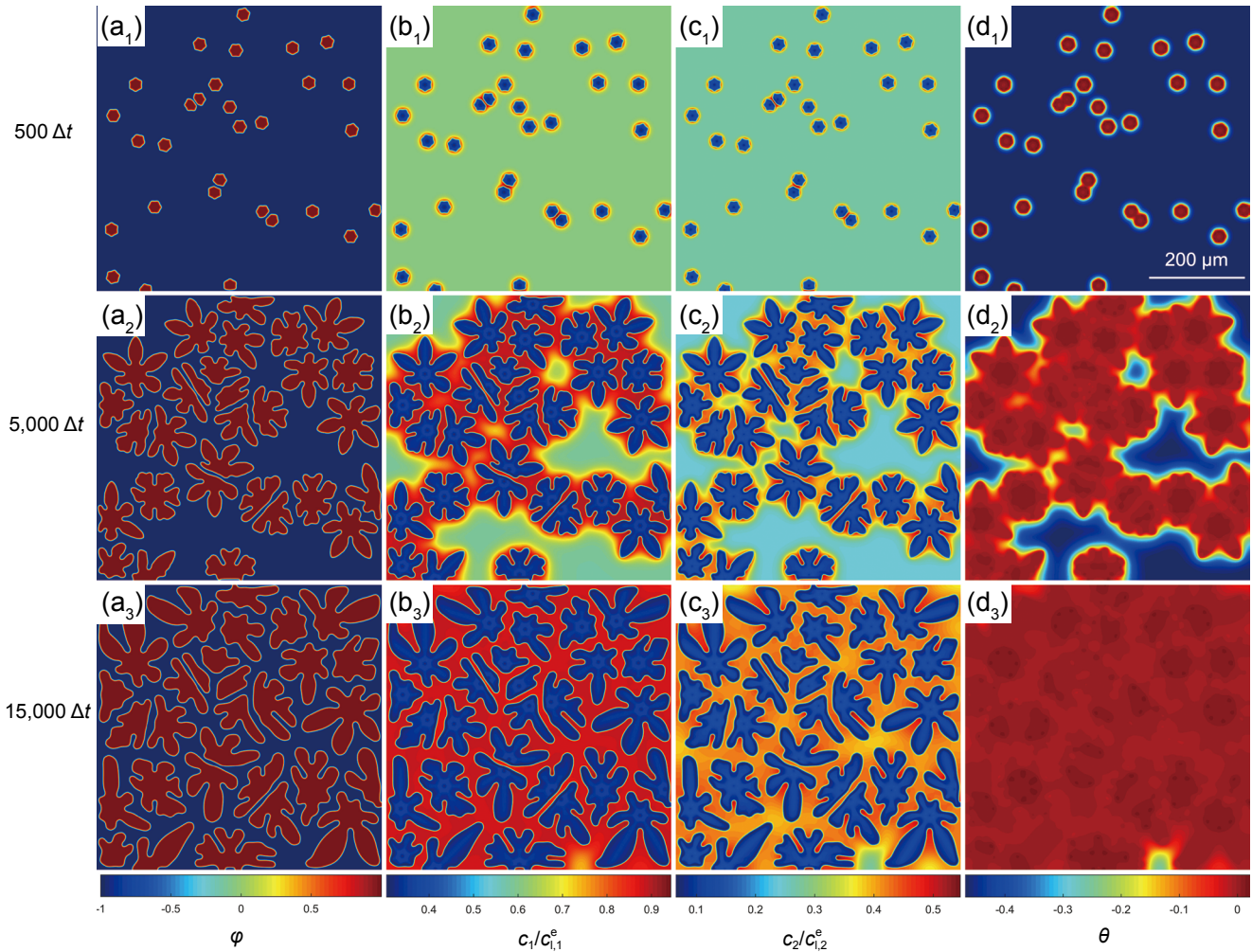


Fig. 2: Simulation results for multi-dendritic growth: (a₁)–(a₃) dendritic morphologies; (b₁)–(b₃) and (c₁)–(c₃) dimensionless concentration distribution of Solute 1 and Solute 2, respectively; (d₁)–(d₃) distribution of dimensionless temperature

3.2 Effect of spatial discretization

In the simulation, the spatial step ($\Delta x/W_0$) not only determines the accuracy of the numerical results but also has a decisive impact on computational efficiency. To select the appropriate spatial step, the variation of average velocity and radius of dendrite tip over time was studied under multiple spatial steps, and the convergence of the model was verified. Figure 3 quantitatively illustrates how the average tip velocity and radius of four dendrite arms with different orientations are affected by the spatial step. Figure 3(a) shows that the average tip velocity of the four different dendrite arms decreases exponentially over time. When the spatial step is small, the free growth stage of dendrites is long. With the increase of the spatial step, the free growth stage of dendrites is significantly

shortened. Meanwhile, the velocity curve during the free growth stage of dendrite gradually becomes unstable and fluctuates as the spatial step increases. Especially when the spatial step is 1.0, it is found that the tip growth rate curve fluctuates obviously. When the spatial step further increases to 1.2, the fluctuation is more drastic. This means that the residual grid noise increases with the increase of spatial step, resulting in measurement error, and then causing the fluctuation of velocity curve. If the spatial step presents too large ($\Delta x/W_0 > 1.0$), the calculation nodes of the interface diffusion layer would reduce, which will have influence on the shape of the dendritic tip. For instance, when $\Delta x/W_0 = 1.2$, the dendrite tip prones to split, as shown in Fig. 3(a). The steady state tip radius is extracted by averaging the value of tip radius

within the last oscillation for each case. The changes of the steady state tip radius as a function of spatial step are shown in Fig. 3(b). It can be seen that when $\Delta x/W_0=0.2$, the tip radius of the dendrite is 27.6002. With the increase of the spatial steps ($\Delta x/W_0=0.4-0.8$), the tip radius gradually stabilizes and changes within a small range. The tip radius increases from 13.33449 to 14.52297 with an error of about 0.04. However,

with the further increase of spatial step to 1.0, the radius value suddenly increases, breaking the stable trend. Therefore, the appropriate spatial step is within the range of 0.4 to 0.8. To achieve a good combination of the computing efficiency and accuracy, all subsequent simulations are performed with the grid spacing of $\Delta x/W_0=0.8$, unless otherwise specified.

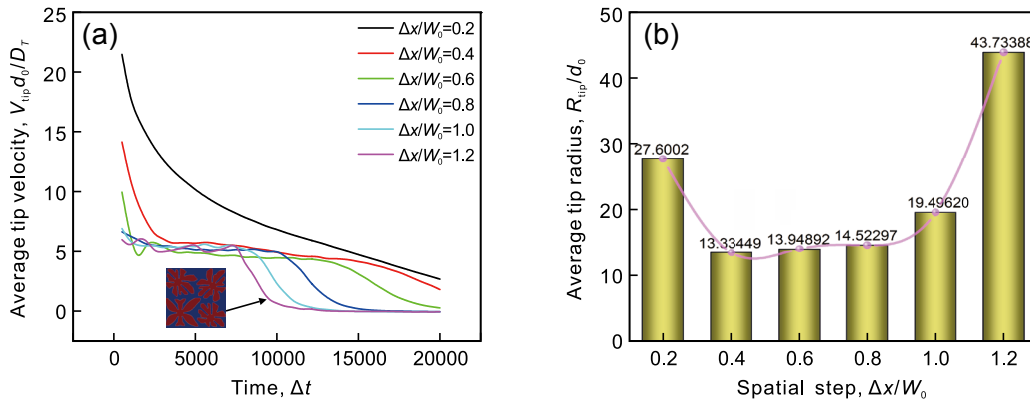


Fig. 3: Time evolution of tip velocity under different spatial steps (a), and variation of average tip radius with spatial step (b)

3.3 Effect of coupling coefficient λ on dendritic growth

According to the equation $W_0=d_0\lambda/a_1$, a_1 is a constant, the thickness W_0 of interface depends on the selection of λ . Therefore, λ also affects the calculation accuracy and efficiency. Previous studies on λ , using Karma model, mainly focus on isothermal solidification of binary single crystal with fcc crystalline structure [14, 33, 36, 37]. The emphasis of this study is on the non-isothermal solidification of ternary alloys with hcp crystalline structure, which is different from the anisotropic of cubic crystals. Therefore, it is necessary to determine the range of λ again. As shown in Fig. 4, the effects of different coupling constants on the tip velocity, for example, solid phase volume fraction, tip radius, and stability coefficient of the dendrite tip, were investigated to obtain the optimal value. Figure 4(a) demonstrates that the dendrite tip velocity increases with the increase of λ , showing a step-like change. In addition, with the increase of λ , the time when the tip velocity of the dendrite in the free growth stage reaches the inflection point gradually advances. When $\lambda=15$, the time is the shortest,

but after further increasing λ , the time continues to extend. Meanwhile, the partial enlarged view of the red rectangle in Fig. 4(b), shows that the solid phase volume fraction is the highest for $\lambda=10$. When $\lambda=20$, the conversion rate of the solid phase volume fraction recedes obviously. With the increase of λ , the conversion rate decreases further, as shown in Fig. 4(b). Figure 4(c) shows the variation of tip radius and stability coefficient ($\sigma^*=2D_T d_0/R^2V$) [36] with different λ . The marginal stability theory points out the critical state between the splitting of dendrite tip and lateral instability, which depends on the dimensionless parameter σ^* . As shown in Fig. 4(c), as λ increases, then the tip radius decreases gradually, then, reaches a plateau region, and finally increases. In contrast, the stability coefficient has an opposite trend with tip radius as the increase of λ . At $\lambda=8, 10, 15$, the slope of the stability coefficient increases slightly, which can be approximately constant, indicating that the stability of the dendrite tip is the best. Therefore, the appropriate λ is within the range of 8 to 15. In the following numerical simulations, $\lambda=10$ was selected.

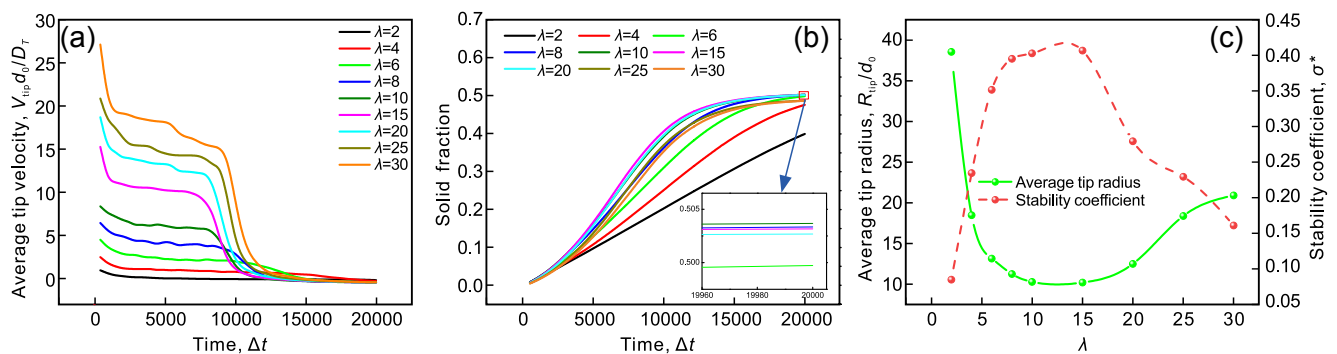


Fig. 4: Time evolution of tip velocity (a) and solid fraction (b) under different coupling parameters λ , and convergence behavior of tip radius and stability coefficient with respect to coupling parameter λ (c)

3.4 Influence of Lewis coefficient on simulation results

The Lewis coefficient (Le) is an important parameter that will influence the dissipation of latent heat during non-isothermal solidification [22, 37]. To investigate the influence of the Lewis coefficient on solidification process, the simulations with various magnitudes of Le were performed for the dendrite growth. The tip velocity as a function of time is given in Fig. 5(a). Generally, the tip velocity increases as Le increases. If Le decreases, the dissipation of latent heat is restrained, so the undercooling at the solid-liquid interface decreases, which will lead to a decrease of dendrite growth rate. In addition, when Le is small, the temperature of some solid phases exceeds the melting point, which results in remelting of some grains and slowing dendrite growth. Meanwhile, a great amount of solute is discharged from dendrite arms due to the competitive growth of dendrites during solidification, which eventually leads to solute enrichment between dendrites, limits the dendrite growth. When Le is high, the thermal diffusivity is larger than the solute diffusivity, so the latent heat of solidification is capable of releasing in time, leading to a faster dendrite growth rate and the vanishes of local remelting phenomenon, and the dendrite enters the coarsening stage ahead of time. The tip radius as a function of Le is shown in Fig. 5(b). In Fig. 5(b), with an increase of Le , the tip radius significantly decreases and gradually tends to be stable. It indicates that with the increase of Le , the influence of thermal driving on the growth of dendrites gradually weakens, and the main driving force for the growth of dendrites changes from thermal diffusion to solute diffusion.

To further analyze the variation of concentration and temperature under different Le , the Line A-A [marked by the black line in the simulated area in Fig. 5(c)] was selected for detailed studies. The crest and trough of the concentration profile along Line A-A shown in Fig. 5(c) ($t=20,000 \Delta t$) match the dendrite and dendritic interval, respectively. When $Le=1$ or 2, the growth rate of dendrites is slower and the solute has enough time to diffuse, so the solute element in the solid phase diffuses more fully and the solute concentration is lower. With the further increase of Le , the growth rate of dendrites increases, which shortens the diffusion time of the solute, so that the solute element in the solid phase is unable to diffuse sufficiently, and the solute concentration gradually increases. In addition, according to the relationship ($c_s/k=c_l$) between the solute concentration and the partition coefficient, the liquid solute concentration gradually increases with the increase of the solute concentration of the solid phase. Figure 5(d) shows the temperature distribution along the Line A-A for different Le . Similar to the Fig. 5(c), at $t=20,000 \Delta t$, the crest and trough of temperature profile also correspond to the dendrite and dendritic interval. Generally, the temperature inside the grain is higher than the temperature of the liquid. With the increase of Le , the temperature difference between inside and outside the crystal decreases, and the temperature field distribution tends to be stable. This is because an increasing amount of latent heat is released as Le rises to 50 and 100. Due to the adiabatic boundary, heat can only accumulate within the system rather than flowing out, thus the temperature distribution tends to become uniform.

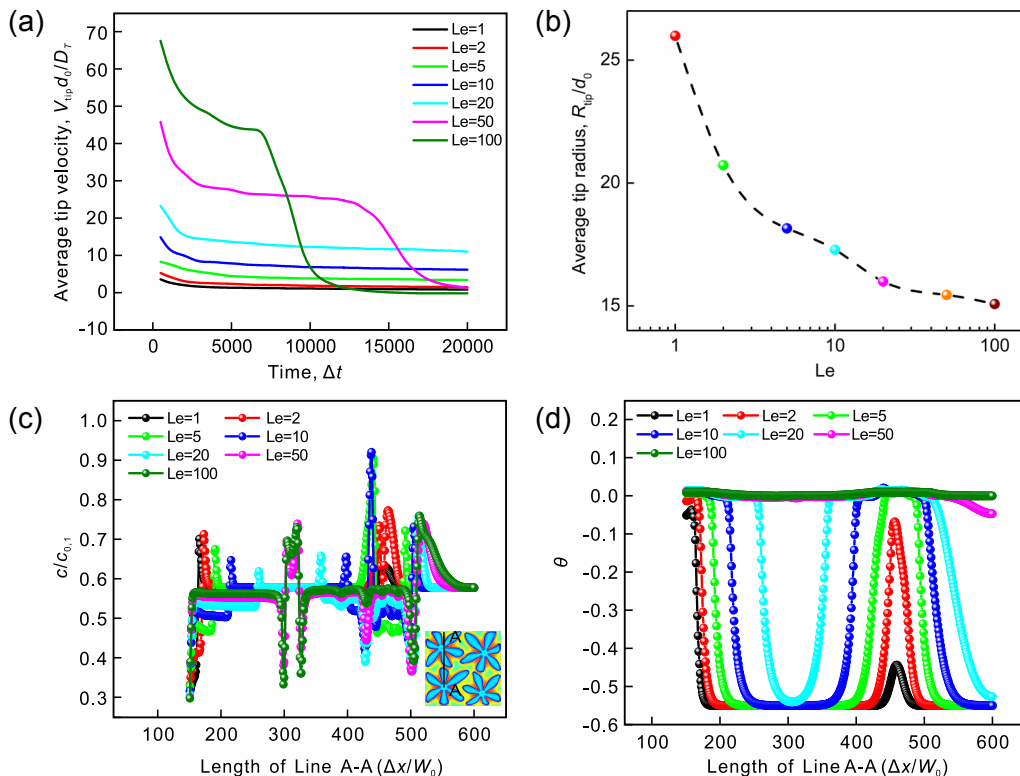


Fig. 5: Influence of different Lewis coefficients on dendrite growth: (a) time evolution of tip velocity; (b) variation of tip radius with Lewis coefficient; (c), (d) concentration and temperature distribution along Line A-A at $t=20,000 \Delta t$, respectively

3.5 Effect of initial undercooling on dendrite growth

Undercooling is the primary driving force for the solidification of liquid metal, which is also an important factor in determining the dendritic morphology. Assuming all other phase-field parameters are fixed, the dendrite morphology evolution under different initial undercooling was studied in this section, as shown in Fig. 6(a). The dimensionless dendrite tip velocities as well as the solid volume fraction versus time for different undercooling during solidification are plotted in Figs. 6(b) and (c). It can be seen when the undercooling is $\Delta=-0.45$, the dendrite size is small and the growth velocity is very slow. As undercooling increases, both the dendrite size and growth velocity increase, and the tip velocity increases rapidly. This shows that the higher the undercooling, the greater the driving force of dendrite growth and the faster the growth rate. During the initial stage of solidification, dendrites grow rapidly and the solid phase volume fraction in the

simulated region rises quickly. Then the solid volume fraction reaches a plateau as the dendrite growth enters the coarsening stage. Figure 6(c) shows that the solid volume fraction increases with the increase of undercooling, which supports the previous conclusion that both the solidification velocity and dendrite growth rate increase as undercooling increases.

The inhomogeneous distribution, enrichment and the increased gradient of solute concentration during solidification can easily cause a series of defects such as black spots and flat grain, which are some of the main reasons for the emergence of brittle fracture. In order to improve the performance of casting part, it is important to investigate and reveal the effect of undercooling on the solute distributions during solidification. The solute distribution along the Line A-A was studied in detail, which is marked by the white line in the simulated area in Fig. 6(a). As shown in Fig. 6(d), the crest and trough of the concentration along A-A line correspond to the dendrite and dendritic interval in Fig. 6(a). It is shown that the concentration

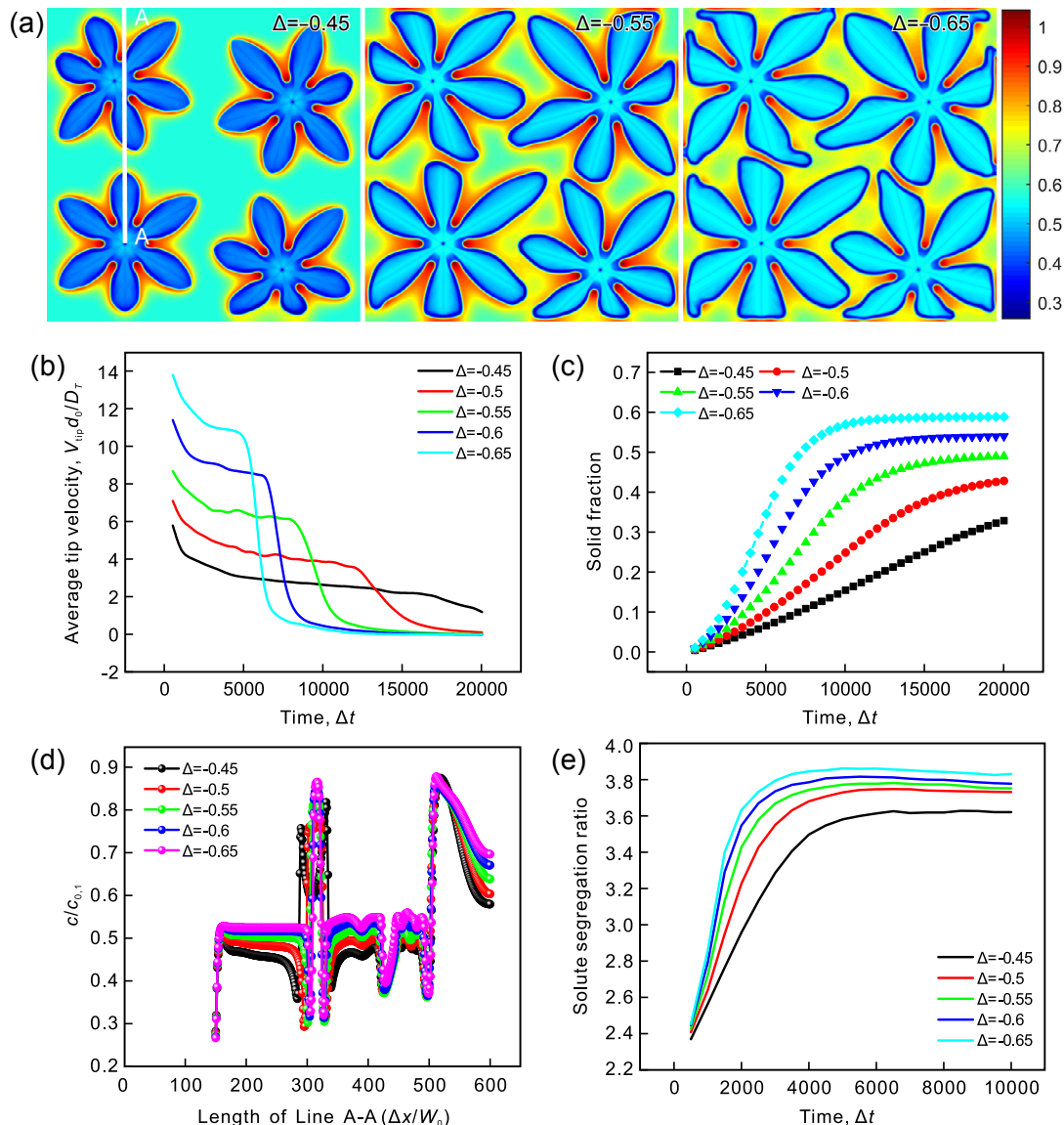


Fig. 6: Influence of different undercooling degrees on dendrite growth: (a) morphology evolution of dendrite; time evolution of tip velocity (b) and solid fraction (c); (d) concentration distribution along Line A-A at $t=20,000 \Delta t$; (e) variation of segregation ratio of solute with time

distribution at solid/liquid interfaces is different under different undercooling. The smaller the undercooling, the slower the growth rate of dendrites, the solute can be fully diffused, and the lower the concentration of solute in the crystal. Under large undercooling, the dendrite growth velocity is fast and the solute can't be diffused sufficiently, resulting in the solute enrichment across the dendrite intervals, which inhibits the release of solute in the solid phase and increases the internal solute concentration. Similarly, the concentration of solute in the liquid phase gradually increases as the undercooling increases. Figure 6(e) shows the segregation ratio of solute with time, which is often used to represent microsegregation in castings. The higher the segregation ratio of solute, the more serious the microsegregation. The segregation ratio is numerically equal to the ratio of the maximum concentration of solute between dendrites to the minimum concentration of solute inside the dendrites. The solute diffusion rate lags far behind the dendrite growth velocity, and the precipitated solute can't fully diffuse into the liquid phase and is enriched at the front of the dendrite. The higher the undercooling, the faster the growth rate of dendrites, the more solutes precipitate into the liquid phase in a unit time, and the higher the concentration of solutes between dendrites, so the segregation rate increases with the increase of the undercooling.

3.6 Simulation of dendritic arms growth with different orientations

In order to better understand the effects of solute diffusion and thermal diffusion on the growth of dendrites with different orientations. The growth behavior of different dendritic arms

was quantitatively studied. Figure 7(a) shows the morphology and the concentration distribution of four dendrites with different orientations. At $t=15,000 \Delta t$, the tip velocity, tip temperature and tip concentration were measured from 1, 2, 3 and 4 arms, respectively. Figures 7(b), (c) and (d) quantitatively illustrate how dendritic arms with different orientations influence each other through solute diffusion and thermal diffusion. Initially, all dendrite arms grow in a free condition. The distance between dendrites is sufficiently large to ensure that each individual dendrite will not be impinged. The interaction energy introduced in Eq. (6) does not affect the growth of dendrites. The thermal diffusion fields and solute diffusion fields of each dendrite have not overlapped with each other. Dendrites grow fast into the melt along the preferred directions corresponding to their given orientation angles. Compared to the other three dendritic arms, there is relatively higher growth velocity for the Arm 4. Meanwhile, combined with Figs. 7(c) and (d), it is found that the tip temperature and concentration of Arm 4 are relatively low at the beginning of solidification. As solidification proceeds, dendrites surrounding thermal field and solute field start to interact and the stage of impingement begins. As the dendrite arms approach each other, the interaction energy (Fig. 1) between the dendrites increases sharply. This suppresses the occurrence of the merger phenomenon between different dendrites. At this stage, it can be observed that the temperature and concentration of the tip of the dendrite Arm 4 change drastically and gradually reach the maximum. With the development of dendrite arms, the interaction energy between dendrites increases significantly. The growth of Arm 1 is blocked by Arm 4, its growth rate

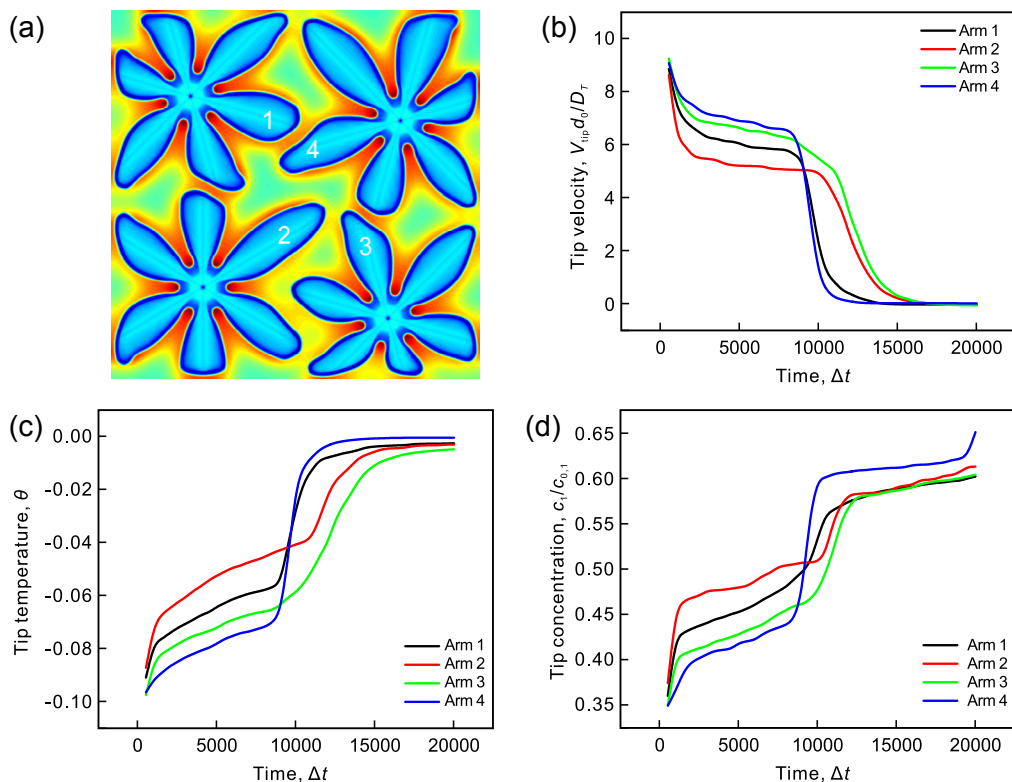


Fig. 7: Morphology evolution of dendrite arms with different orientations (a), time evolution of tip velocity (b), tip temperature (c), and tip concentration (d) of different dendrite arms

suddenly drops, and a large amount of heat and solute begin to accumulate at its tip. The growth rate of Arm 3 also begins to be affected by dendrite, and gradually declines. In addition, because of the larger growth space at the tip of the Arm 2 and its smaller interaction energy with other dendrites, the free growth stage of the Arm 2 is the longest. Subsequently, the tip growth velocity of all those four arms will eventually get close to zero, with the increase of tip temperature and concentration, as shown in Figs. 7(b), (c) and (d), which hinders the dendritic tip growth. However, although the dendritic tip almost stops growing, the solidification is still evidently in progress since the dendritic tip is getting coarsened.

3.7 Polycrystalline growth kinetics

The growth kinetics of multiple dendrites, especially the evolution of solid volume fraction, is a key problem in solidification. JMAK theory^[27-29] and Starink phenomenological theory^[38] are classical theories on the growth kinetics of multiple dendrites. In JMAK theory, the transformed volume fraction of multiple particles with time satisfies the following relationship:

$$f(t) = 1 - e^{-x_c(t)} \quad (11)$$

where t represents the solidification time, and $x_c(t)$ is the extended volume fraction when ignoring the inter particle collision, which can be expressed as:

$$x_c(t) = Mt^n \quad (12)$$

In Eq. (12), M is a constant, and n represents the Avrami

index describing particle growth, which can be expressed as $n=qd+X$, d is the dimension of space, q equals 0.5 for diffusion controlling growth and 1 for the interface controlling the grain growth, X equals 0 for site saturation nucleation and 1 for nucleation with a constant rate. Because of the complexity of dendrite morphology, although the dendrite growth in undercooled melts is a diffusion-controlled process, it is unreasonable to think that index $n=1$ for the two-dimensional dendrite growth. Brener et al.^[39] used the parabola shape approximation to replace the needle-like dendrite arm without side branches, and found that the dendritic area in two dimensions increased with time was proportional to $t^{1.5}$. However, there is still a lack of reliable test for the accuracy of this simple assumption. Therefore, the growth kinetics of a single smooth needle dendrite arm was simulated to verify the results.

For a dendrite with simple morphology, the relationship between the solid fraction $f_c(t)$ and the time of free growth is exponential, that is, $f_c(t) = M_0 t^m$, where m is the growth exponent and M_0 is a shape factor. The growth kinetics of single crystal under different initial undercooling was studied by using this equation, and the results are shown in Fig. 8. It can be seen from Figs. 8(a) and (b) that under different initial undercooling conditions, the grain size changes greatly, but the growth index curves of different dendrites are basically parallel, which indicates that the index m is less affected by the dendrite morphology. The results are in good agreement with those of Brener et al.^[39,40]. For the non-isothermal growth of a single dendrite at $\Delta = -0.55$, the dimensionless time

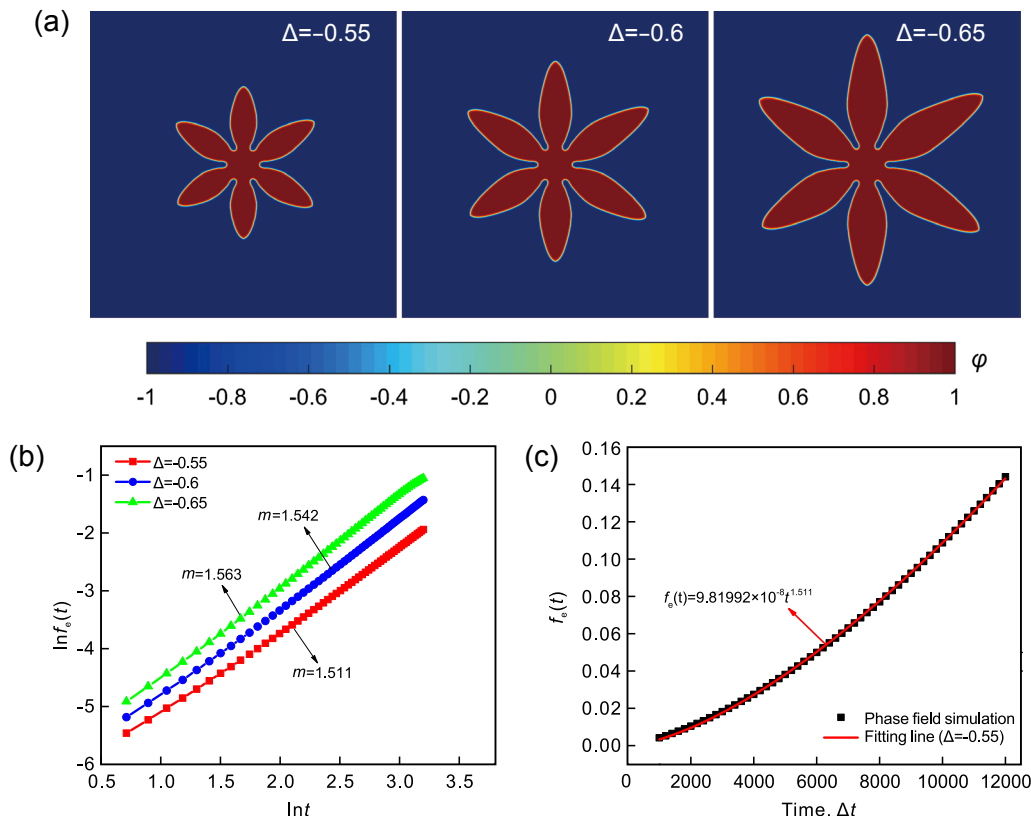


Fig. 8: Under different undercooling, dendrite morphology (a), single dendritic growth index curve (b), and transformed fraction versus time for single dendrite at $\Delta = -0.55$ (c), and red solid line is the best fitting function $f_c(t) = 9.81992 \times 10^{-8} t^{1.511}$

varying data of transition fraction obtained in the simulation is fitted by the formula $f_c(t)=M_0t^m$, and the results are shown in Fig. 8(c). The growth index $m=1.511$ and $M_0=9.81992\times 10^{-8}$ obtained by fitting will be used in later polycrystalline growth dynamics. It is worth noting that $M=M_0N$ in the kinetics study of polycrystalline growth, where N is the number of nuclei.

Although the growth kinetics of single crystal is very close to the theoretical value, polycrystalline solidification is more complex than single crystal solidification, involving competitive growth of dendrites, soft impact effect and latent heat release. Therefore, it is necessary to further analyze the growth kinetics of polycrystal. Here, the method of site saturation nucleation was selected to simulate the random growth of 30 grains. To eliminate the influence of the nucleation position on the simulation, the average value of 5 simulations was extracted. It can be seen from Fig. 9(a) that the Avrami index of polycrystalline growth keeps stable at the starting time, and then decreases gradually with the dendrite growing up. The main reason is that at the initial stage of growth, the growth space of dendrites is sufficient, and there is no collision with each other. Their Avrami index is consistent with that of single crystals. With the increase of dendrite size, the competitive growth between dendrites is intensified, and the mutual blocking effect is enhanced. Meanwhile, it can be

seen from Fig. 9(b) that there is a big deviation between the simulation results of growth kinetics and JMAK theory. Many scholars have studied the reasons for such deviation and found that the soft collision effect and mutual blocking effect of particles in the growth progress were the main reasons [41-45].

Considering the different orientations and anisotropies of particles, Starink et al. [38] and Kooi et al. [45] took into account the blocking effect and proposed a phenomenological equation between the transformed volume fraction and time for multiple particles:

$$\frac{df}{df_c}=(1-Af)^\mu \tag{13}$$

$$\frac{df}{df_c}=\frac{1-f}{(1+bf^2)^2} \tag{14}$$

where A , μ and b are constant. When $A=1$, $\mu=1$ or $b=0$, the two equations revert to the JMAK equation. Equations (13) and (14) are used to compare the phase-field simulation results of polycrystalline growth dynamics with Kooi equation and Starink equation, as shown in Fig. 10. It is found that the simulated results are very close to the theoretical value when considering the soft collision effect and the mutual blocking effect caused by dendrite arbitrary orientation.

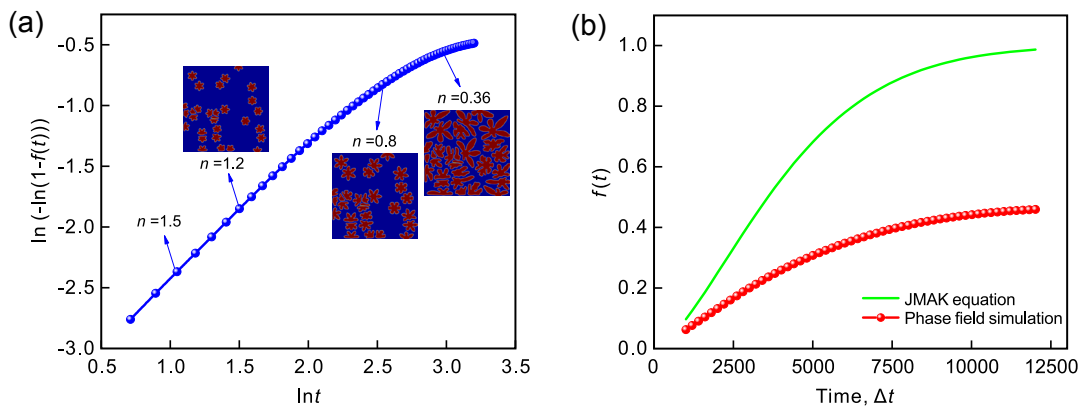


Fig. 9: Avrami exponential curve (a), and growth kinetics curve of multi-dendrite at $\Delta=-0.55$ (b)

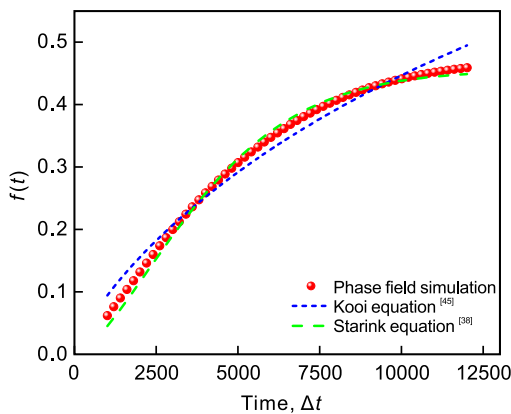


Fig. 10: Curve of transformation fraction with time obtained by phase-field simulation and theoretical fitting. The green dash line is based on Eq. (13) with $A=0.455$ and $\mu=1.03$. The blue dash lines are based on Eq. (14) with $b=5.0001$

3.8 Comparison between experiment and simulation

The solidification structure of ternary Mg-6Gd-2Zn (wt.%) alloy was simulated using the model under the undercooling of 0.65. In this alloy, due to the low solute content, the solute interactions between different species are ignored. For the Mg-6Gd-2Zn (wt.%) alloy, the exact parameters for calculation are as follows: $k_1=0.35$, $k_2=0.16$, $|m|=3 \text{ K}\cdot(\text{wt.}\%)^{-1}$, $\Gamma=0.37 \text{ K}\cdot\mu\text{m}$, $T_m=921 \text{ K}$, $c_p=2.35 \text{ J}\cdot(\text{kg}\cdot\text{K})^{-1}$, $L=610 \text{ J}\cdot\text{kg}^{-1}$, $\rho=31.74 \text{ g}\cdot\text{cm}^{-3}$, $\kappa=156 \text{ W}\cdot(\text{m}\cdot\text{K})^{-1}$, $D_{\text{Gd}}=1.4\times 10^{-9} \text{ m}^2\cdot\text{s}^{-1}$, $D_{\text{Zn}}=5.4\times 10^{-9} \text{ m}^2\cdot\text{s}^{-1}$ [4, 16]. Figure 11(a) shows the simulation results of the ternary Mg-6Gd-2Zn (wt.%) alloy. Comparing the simulation results with the experimental results in Fig. 11(b) [46], it can be found that the microstructure of simulation results is in good agreement with the actual pattern, verifying the validity of the phase-field model.

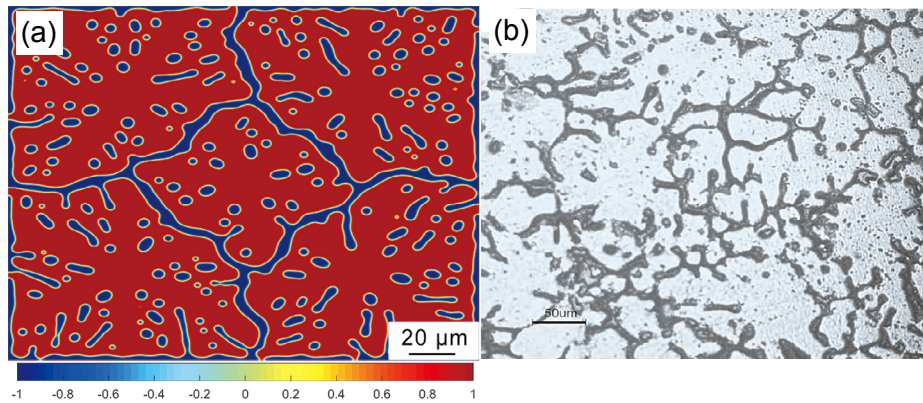


Fig. 11: Simulation result of phase-field method (a) and experimental result (b) of Mg-6Gd-2Zn (wt.%) alloy ^[46]

4 Conclusions

In this work, the multi-dendrites growth in non-isothermal solidification was studied by establishing a polycrystalline and multicomponent phase-field model which coupled with temperature field. The simulation results suggest the following conclusions:

- (1) A near steady-state tip velocity and tip radius is obtained when spatial step range is between 0.4 and 0.8.
- (2) The reasonable value range for λ is between 8 and 15. The optimal solution can be obtained when $\lambda=10$.
- (3) The larger the Lewis coefficient, the more conducive to the release of solidification latent heat, the faster the growth velocity of dendrites, and the more stable the tip radius, which increases the solid phase fraction and solute concentration, and leads to a more uniform temperature distribution.
- (4) With the increase of the initial undercooling, the growth velocity of dendrites is obviously accelerated, and the solid fraction also increases. The higher the undercooling, the higher the solute concentration, the larger the segregation ratio and the more severe the microsegregation.
- (5) With the growth of dendrites, the interaction potential between dendrites increases, the growth velocity of dendrites decreases, and the tip temperature and concentration increase.
- (6) The transformation kinetics of multiple dendrites growth is investigated using phase-field simulation and the result shows good agreement with that of the phenomenological theory. The prediction result of the transformation kinetics of polycrystalline solidification by JMAK theory shows relatively larger than the phase-field simulation result due to the neglect of the soft collision effect and mutual blocking among dendrites. In addition, the solidification process of Mg-6Gd-2Zn (wt.%) alloy was simulated, and the dendrite morphology is consistent with the experimental results.

Acknowledgements

The work was financial supported by the National Natural Science Foundation-Youth Science Foundation Project (No. 51901208), the Henan University Key Scientific Research Project (No. 20B430020), the Key Scientific

and Technological Projects in Henan Province (Nos. 202102210016, 202102210272), and the Major Innovation Project of Zhengzhou City (No. 23101000010).

References

- [1] Chen L Q, Zhao Y H. From classical thermodynamics to phase-field method. *Prog. In Mater. Sci.*, 2022, 124: 100868. <https://doi.org/10.1016/j.pmatsci.2021.100868>.
- [2] Moelans N, Blanpain B, Wollants P. An introduction to phase-field modeling of microstructure evolution. *Calphad*, 2008, 32(2): 268–294.
- [3] Dong X L, Xing H, Weng K R, et al. Current development in quantitative phase-field modeling of solidification. *J. Iron Steel Res. Int.*, 2017, 24(9): 865–878.
- [4] Wang Y B, Wei M G, Liu X T, et al. Phase-field study of the effects of the multi-controlling parameters on columnar dendrite during directional solidification in hexagonal materials. *Eur. Phys. J. E*, 2020, 43(7): 11964.
- [5] Wang J J, Wang B, Chen L Q. Understanding, predicting, and designing ferroelectric domain structures and switching guided by the phase-field method. *Annu. Rev. Mater. Res.*, 2019, 49(1): 1–26.
- [6] Zhang A, Guo Z P, Jiang B, et al. Multiphase and multiphysics modeling of dendrite growth and gas porosity evolution during solidification. *Acta Mater.*, 2021, 214(3): 117005.
- [7] Wheeler A A, Boettinger W J, McFadden G B. Phase-field model for isothermal phase transitions in binary alloys. *Phys. Rev. A*, 1992, 45(10): 7424.
- [8] Kim S G, Kim W T. Phase-field modeling of rapid solidification. *Mater. Sci. Eng. A*, 2001, 304: 281–286.
- [9] Böttger B, Eiken J, Steinbach I. Phase field simulation of equiaxed solidification in technical alloys. *Acta Mater.*, 2006, 54(10): 2697–2704.
- [10] Li J J, Wang Z J, Wang Y Q, et al. Phase-field study of competitive dendritic growth of converging grains during directional solidification. *Acta Mater.*, 2012, 60(4): 1478–1493.
- [11] Almgren R F. Second-order phase field asymptotics for unequal conductivities. *SIAM J. Appl. Math.*, 1999, 59(6): 2086–2107.
- [12] Karma A. Phase-field formulation for quantitative modeling of alloy solidification. *Phys. Rev. Lett.*, 2001, 87(11): 115701.
- [13] Ohno M, Matsuura K. Quantitative phase-field modeling for dilute alloy solidification involving diffusion in the solid. *Phys. Rev. E*, 2009, 79(3): 031603.

- [14] Xing H, Ji M Y, Dong X L, et al. Growth competition between columnar dendrite and degenerate seaweed during directional solidification of alloys: Insights from multi-phase field simulations. *Mater. Design*, 2020, 185: 108250.
- [15] Tourret D, Karma A. Growth competition of columnar dendritic grains: A phase-field study. *Acta Mater.*, 2015, 82: 64–83.
- [16] Wang Y B, Jia S S, Wei M G, et al. Coupling in situ synchrotron X-ray radiography and phase-field simulation to study the effect of low cooling rates on dendrite morphology during directional solidification in Mg-Gd alloys. *J. Alloys Compd.*, 2020, 815: 152385.
- [17] Zhang A, Du J L, Guo Z P, et al. Evolution of specific interface area during solidification: A three-dimensional thermosolutal phase-field study. *Comput. Phys. Commun.*, 2021: 108042.
- [18] Ofori-Opoku N, Provatas N. A quantitative multi-phase field model of polycrystalline alloy solidification. *Acta Mater.*, 2010, 58(6): 2155–2164.
- [19] Chen Y, Qi X B, Li D Z, et al. A quantitative phase-field model combining with front-tracking method for polycrystalline solidification of alloys. *Comp. Mater. Sci.*, 2015, 104: 155–161.
- [20] Yang C, Xu Q Y, Liu B C. GPU-accelerated three-dimensional phase-field simulation of dendrite growth in a nickel-based superalloy. *Comp. Mater. Sci.*, 2017, 136: 133–143.
- [21] Gong T Z, Chen Y, Cao Y F, et al. Fast simulations of a large number of crystals growth in centimeter-scale during alloy solidification via nonlinearly preconditioned quantitative phase-field formula. *Comp. Mater. Sci.*, 2018, 147: 338–352.
- [22] Wu J, Guo Z P, Luo C. Development of a parallel adaptive multigrid algorithm for solving the multi-scale thermal-solute 3D phase-field problems. *Comp. Mater. Sci.*, 2018, 142: 89–98.
- [23] Ren J K, Chen Y, Xu B, et al. A vector-valued phase field model for polycrystalline solidification using operator splitting method. *Comp. Mater. Sci.*, 2019, 163: 37–49.
- [24] Wang M Y, Xu Y J, Zheng Q W, et al. Dendritic growth in Mg-based alloys: Phase-field simulations and experimental verification by X-ray synchrotron tomography. *Metall. Mater. Trans. A*, 2014, 45(5): 2562–2574.
- [25] Yang M, Xiong S M, Guo Z P. Effect of different solute additions on dendrite morphology and orientation selection in cast binary magnesium alloys. *Acta Mater.*, 2016, 112: 261–272.
- [26] Shuai S S, Guo E Y, Zheng Q W, et al. Three-dimensional α -Mg dendritic morphology and branching structure transition in Mg-Zn alloys. *Mater. Charact.*, 2016, 118: 304–308.
- [27] Avrami M. Kinetics of phase change. I General theory. *J. Chem. Phys.*, 1939, 7(12): 1103–1112.
- [28] Avrami M. Kinetics of phase change. II Transformation-time relations for random distribution of nuclei. *J. Chem. Phys.*, 1940, 8(2): 212–224.
- [29] Rollett A D, Srolovitz D J, Doherty R D, et al. Computer simulation of recrystallization in non-uniformly deformed metals. *Acta Mater.*, 1989, 37(2): 627–639.
- [30] Elder K R, Grant M, Provatas N, et al. Sharp interface limits of phase-field models. *Phys. Rev. E*, 2001, 64(2): 021604.
- [31] Amoozeaei M, Gurevich S, Provatas N. Orientation selection in solidification patterning. *Acta Mater.*, 2012, 60(2): 657–663.
- [32] Yu F Y, Wei Y H. Phase-field investigation of dendrite growth in the molten pool with the deflection of solid/liquid interface. *Comp. Mater. Sci.*, 2019, 169: 109128.
- [33] Ohno M. Quantitative phase-field modeling of nonisothermal solidification in dilute multicomponent alloys with arbitrary diffusivities. *Phys. Rev. E*, 2012, 86(5): 051603.
- [34] Karma A, Rappel W J. Phase-field method for computationally efficient modeling of solidification with arbitrary interface kinetics. *Phys. Rev. E*, 1996, 53(4): 3017–3020.
- [35] Karma A, Rappel W J. Quantitative phase-field modeling of dendritic growth in two and three dimensions. *Phys. Rev. E*, 1998, 57(4): 4323–4349.
- [36] Ramirez J C, Beckermann C. Examination of binary alloy free dendritic growth theories with a phase-field model. *Acta Mater.*, 2005, 53(6): 1721–1736.
- [37] Rosam J, Jimack P K, Mullis A M. Quantitative phase-field modeling of solidification at high Lewis coefficient. *Phys. Rev. E*, 2009, 79(3): 30601.
- [38] Starink M J. On the meaning of the impingement parameter in kinetic equations for nucleation and growth reactions. *J. Mater. Sci.*, 2001, 36(18): 4433–4441.
- [39] Brener E, Müller-Krumbhaar H, Temkin D. Kinetic phase diagram and scaling relations for stationary diffusional growth. *Europhys. Lett.*, 1992, 17(6): 535–540.
- [40] Li J J, Wang J C, Xu Q, et al. Comparison of Johnson-Mehl-Avrami-Kolmogorov (JMAK) kinetics with a phase field simulation for polycrystalline solidification. *Acta Mater.*, 2007, 55(3): 825–832.
- [41] Weinberg M C, Birnie III D P. Avrami exponents for transformations producing anisotropic particles. *J. Non-Cryst. Solids*, 1996, 202(3): 290–296.
- [42] Weinberg M C, Birnie III D P, Shneidman V A. Crystallization kinetics and the JMAK equation. *J. Non-Cryst. Solids*, 1997, 219(97): 89–99.
- [43] Pusztai T, Gránásy L. Monte Carlo simulation of first-order phase transformations with mutual blocking of anisotropically growing particles up to all relevant orders. *Phys. Rev. B*, 1998, 57(22): 14110–14118.
- [44] Pradell T, Crespo D, Clavaguera N, et al. Diffusion controlled grain growth in primary crystallization: Avrami exponents revisited. *J. Phys.: Condens. Matter*, 1998, 10(17): 3833–3844.
- [45] Kooi B J. Monte Carlo simulations of phase transformations caused by nucleation and subsequent anisotropic growth: Extension of the Johnson-Mehl-Avrami-Kolmogorov theory. *Phys. Rev. B*, 2004, 70(22): 155–163.
- [46] Guo Y C, Cheng L, Wu Y X. Microstructure and phase analysis of Mg-Gd-Zn alloys. *Chinese Journal of Rare Metals*, 2014, 38(4): 603–608. (In Chinese)